

Article

Microstructure and Mechanical Property Evolution of Robotic Friction Stir-Welded Al–Li Alloys

Yisong Wang^{1,2}, Haitao Jiang^{1,*}, Xiaoyan Wu¹ and Qiang Meng²

¹ National Engineering Research Center for Advanced Rolling and Intelligent Manufacturing, University of Science and Technology Beijing, Beijing 100083, China

² AVIC Manufacturing Technology Institute, Beijing 100024, China

* Correspondence: jianght@ustb.edu.cn

Abstract: 2198 aluminum–lithium alloy was friction stir-welded with a KUKA Robot integrated with a compact friction stir-welding head with a rotation speed of 800 rpm at different welding speeds. The real-time tool force in the three directions of F_x , F_y and F_z was measured with a load sensor. Mechanical properties and microstructure evolution were investigated systematically. The results showed that F_z force increased from 3.2 kN to 8.5 kN as welding speed increased from 50 mm/min to 500 mm/min. Ultimate tensile strength of 383 MPa, 88% of base metal, was obtained when the welding speed was 100 mm/min. The nugget zone consisted of refined grains with an average size of 4 μm . TEM investigation demonstrates that T1 precipitation predominated in the base metal and disappeared in the nugget zone, as a small amount of δ' was retained. The W-shape hardness profile in all weldments and higher welding speed lead to a higher hardness value.

Keywords: robotic friction stir-welding; Al–Li alloy; welding force; mechanical property; microstructure



Citation: Wang, Y.; Jiang, H.; Wu, X.; Meng, Q. Microstructure and Mechanical Property Evolution of Robotic Friction Stir-Welded Al–Li Alloys. *Crystals* **2023**, *13*, 582. <https://doi.org/10.3390/cryst13040582>

Academic Editor: Pavel Lukáč

Received: 26 February 2023

Revised: 22 March 2023

Accepted: 23 March 2023

Published: 29 March 2023



Copyright: © 2023 by the authors. Licensee MDPI, Basel, Switzerland. This article is an open access article distributed under the terms and conditions of the Creative Commons Attribution (CC BY) license (<https://creativecommons.org/licenses/by/4.0/>).

1. Introduction

Increasing payload and fuel efficiency of aircraft has become a major issue for aerospace and led to development of materials with highly specific mechanical properties. Al–Li alloys have received much attention for lightweight aircraft because of their low density, improved specific strength, and high stiffness-to-weight ratio [1–4]. 2198 aluminum alloy is a third generation Al–Li alloy with high stiffness, strength, and excellent low-temperature toughness. It is predominately utilized in aviation and space industries [5,6]. 2198 Al–Li alloy is a kind of precipitation-strengthening aluminum alloy which is hard to weld using conventional fusion-welding techniques. Friction stir-welding (FSW) is a revolutionary solid-state welding technology that has been successfully utilized in the space, aviation, shipbuilding, and automotive industry [7–9]. It is considered a green and efficient welding method with high joint quality and small welding deformation, suitable for the connection of aluminum alloys, especially the conventional fusion-welding of non-weldable high-strength aluminum alloys [10–14]. With the development of intelligence, industrial robots have become an important medium of intelligent manufacturing, with the ability to replace traditional gantry machinery; FSW robots have emerged, showing intelligence, flexibility, and automation.

Recently, several papers were published regarding the microstructural and mechanical properties of Al–Li alloys undergoing FSW. Hao presented results of tensile and bending mechanical properties as a function of processing parameters in 1420 alloy [15]. The optimized combinations of various welding parameters (pin rotation speed, welding speed and welding pressure) were identified. By comparison of the heat inputs during the welding process at different parameter combinations, the relationship between the grain size in the stirred zone (SZ) and the welding parameters was established. Cavaliere studied the effect of anisotropy on mechanical and fatigue properties of 2198 Al–Li plates undergoing FSW [16,17]. Both the L- and T-welds show a similar behavior in crack initiation and growth,

leading to the conclusion that the FSW process eliminates the effect of rolling direction on the fatigue properties of the welds, and Chen paid attention to plastic flow and ductile rupture of 2198 undergoing FSW [18]. Two microscopic fracture mechanisms are identified: fibrous fracture involving grain boundary decohesion and dimple fracture. Observed fracture modes depend on specimen geometry (notches increase stress triaxiality and favor dimple fracture) but also on loading direction. Loading along the rolling direction leads to predominant fibrous fracture. Cisko A. R. et al. [19] conducted process research on 2099 aluminum–lithium alloy, revealing the effects of tool rotational rates and transverse speeds on the microstructure and tensile strength of joints. A strong correlation between tool transverse speed and tensile strength and ductility was found. Specifically, the elongation to failure and ultimate tensile strength increased as the transverse speeds increased, due to a direct decrease in the heat input. However, elongation to failure and ultimate tensile strength were less dependent on the rotational rate, since adequate material mixing was achieved and strain rate sensitivity was negligible at these strain rates. Peng Chen [20] studied the correlation of temperature evolution, microstructure, and mechanical properties of individual regions in 2195-T8 Al–Li alloy joints made with FSW. It was shown that peak temperature was 358–376 °C in the heat-affected zone (HAZ) where joint failure occurred due to the dissolution and coarsening of T1 and development of a coarse grain boundary phase and precipitate-free zones (PFZs). Peak temperature of the thermo-mechanically affected zone (TMAZ) ranged from 376 °C to 401 °C, leading to complicated precipitation behavior. The dissolution and coarsening of precipitates resulted in joint softening, while a layer of fine equiaxed grains at the interface of the AS-TMAZ/NZ increased the hardness of this region. However, all this work was finished with gantry machines rather than industrial robots. Robotic friction stir-welding has the advantages of flexibility and convenience to integrate into the production line. It has a broad application prospect in the manufacture of aviation curved surface structures. Moreover, Al–Li aluminum alloy has an obvious weight reduction effect, which has been widely used in aircraft fuselage mechanisms. However, there is limited research on Al–Li aluminum alloy undergoing FSW. The microstructure and performance of Al–Li alloy FSW joints formed using this new welding method of robotic FSW is unclear. At the same time, due to the relatively small structural rigidity of the robot compared to the gantry equipment, during the welding process, problems such as welding path deviation or even welding defects are prone to occur due to excessive load [21].

In order to provide basic data for academic research and engineering applications, the microstructure and mechanical property evolution of robotic FSW Al–Li alloys were investigated systematically. A 2 mm AA 2198-T8 aluminum alloy was welded using an articulated robot with a FSW head mounted on the sixth axis. The welding force during processing was recorded by sensors in order to offer a reference point for flexibility investigation of robotic FSW. The microstructure evolution and mechanical properties caused by welding speed were investigated in detail. All the results will provide an important basis for the application and promotion of the robotic FSW manufacturing process in the field of Al–Li alloy material connection and aviation manufacturing.

2. Experimental

A 2 mm thickness 2198 Al–Li alloy plate was used; its chemical compositions are given in Table 1.

Table 1. Chemical compositions of 2198-T8 Al–Li alloy (mass, wt. %).

Li	Si	Fe	Cu	Mn	Mg	Cr	Zn	Ag	Al
0.98	0.04	0.026	3.56	0.3	0.72	<0.01	0.34	0.086	balance

An articulated industrial KUKA Titan robot, offering a lift force of 1000 Kg, was utilized, as shown in Figure 1. The FSW head with an electric spindle was developed in the China FSW Center, affiliated with the AVIC Manufacturing Technology Institute (MTI). A force sensor was installed in the appropriate position to measure the welding force of

the tool in real-time, which was denoted as F_x , F_y , and F_z , respectively. The tool consisted of a concave shoulder and tapered pin; the diameter of the shoulder was 8 mm, and the length of the pin was 1.7 mm. A schematic diagram of the welding principle is provided in Figure 2.



Figure 1. KUKA Titan industrial robot.

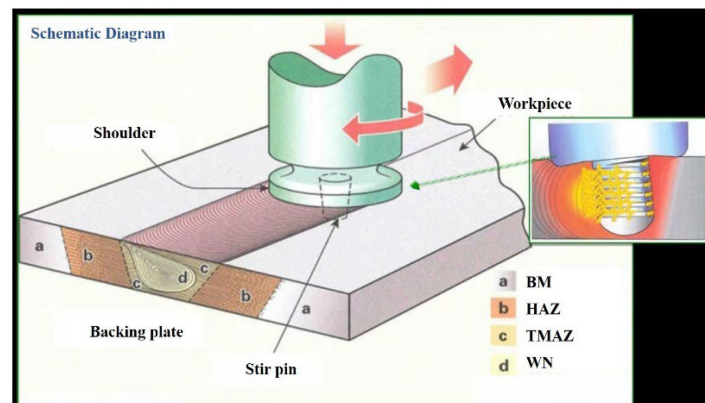


Figure 2. Schematic diagram of welding principle.

A 100×150 mm plate was used to butt-weld, and the joining surface was machined to remove the oxidation layer and cleaned with ethanol. The rotation speed was 800 rpm, and travelling speeds were 50 mm/min, 75 mm/min, 100 mm/min, 200 mm/min, 300 mm/min, 400 mm/min, and 500 mm/min. After welding, the specimens were cut perpendicular to the welding direction with an electrical discharge cutting machine, and the tensile test and bending test specimens were prepared according to ISO4136 and ISO5173. The tensile test was carried out on a Z100 universal tensile testing machine. The three-point bending test was implemented on an EMSYS electric universal materials testing machine, with a bending rate of 2 mm/min and an elbow diameter of 10 mm, recording the bending angle while fracture emerged. The metallographic examination was performed using standard techniques, including sectioning along the centerline of the weld, grinding, polishing, and etching with Keller's reagent for 40 s. The microstructure of the joints was observed with Leica DM6000M optical microscopy (Leica, Weizl, Germany). Hardness measurement was carried out in centerline; a 432VD Vicky hardness machine (Wilson, Chicago, IL, USA) was used to measure the hardness along the thickness of the crossing section at intervals of 1 mm. The testing force was 250 g and dwell time was 10 s. An electron back-

scatter diffraction (EBSD) test and fracture surface observation was undertaken via Philips X130 scanning electron microscopy (Philips, Amsterdam, The Netherlands) integrated with an EBSD system. Transmission electron microscope (TEM) samples of the different welding zones, including the BM, HAZ, and SZ, were carefully taken from the plane, which was perpendicular to the normal direction. The thin foil specimens for TEM observation were prepared with the twin-jet electrolytic polishing method using a solution of 5% HClO₄ + 95% C₂H₅OH. Transmission electron microscopy (TEM) observation of weldment was conducted on a ZEISS SUPRA 55 (ZEISS, Jena, Germany).

3. Results and Discussion

3.1. Real-Time Force Variation

The real-time F_x, F_y, and F_z force of 50 mm/min, 100 mm/min, 200 mm/min and 500 mm/min weldments are shown in Figure 3. During FSW, the F_x and F_y force varied within a relatively small scope, and welding speed imposed little effect on these forces. However, F_z altered significantly and decreased sharply with the increase in welding speed. The force kept at a constant level of 3.8 kN at the condition of 50 mm/min, and 8.4 kN at 500 mm/min. It suggested that fast welding speed leads to high F_z force.

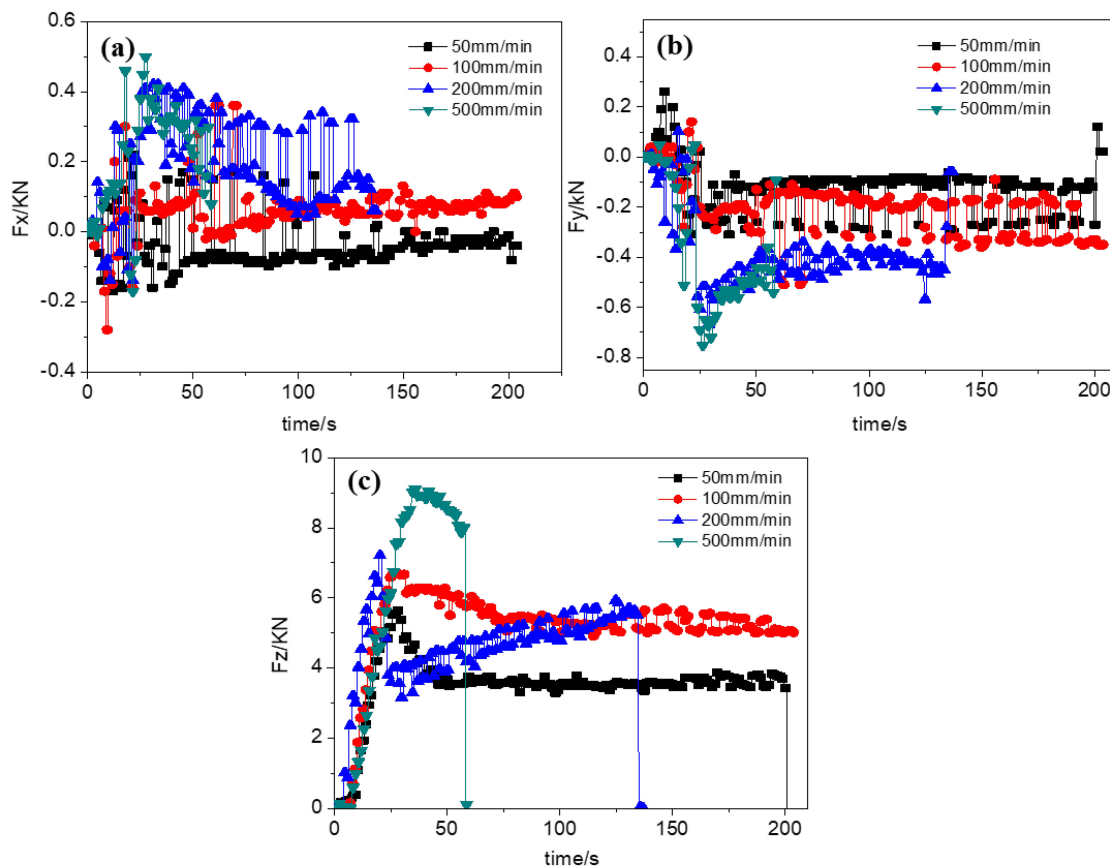


Figure 3. F_x, F_y, and F_z forces during robotic FSW of 2198–T8 Al–Li alloy. (a) F_x force; (b) F_y force; (c) F_z force.

The FSW process was a combination of friction heat and severe plastic deformation. The heat generation was calculated by Equation (1) proposed by Chao and Qi [22].

$$Q = \frac{\pi\omega\mu F(R_{shoulder}^2 + R_{shoulder}R_{pin} + R_{pin}^2)}{45(R_{shoulder} + R_{pin})} \quad (1)$$

where Q is overall friction heat generation during the process; ω is rotation speed; μ is the friction coefficient; $R_{shoulder}$ is the radius of shoulder and R_{pin} is the radius of pin; F is

forging force imposed by the tool (in this equation F is regarded as constant). In this study, F differed from each other at different welding speeds.

Arbegas and Hartley [23] clarified the effect of welding parameters on temperature and established an equation to illuminate the relationship between maximum temperature T ($^{\circ}\text{C}$), rotation speed ω (rpm), and welding speed v (mm/min), as given in Equation (2).

$$\frac{T}{T_m} = k \left(\frac{\omega^2}{v} \right)^\alpha \quad (2)$$

T is maximum temperature during welding; T_m is the melting point of aluminum alloys; and k is scale factor. For aluminum alloys, k is in the range of 0.65–0.75; exponent α varied from 0.04 to 0.06.

It could be speculated that the peak temperature decreased as the welding speed became faster, because less friction heat per unit length was generated and the softened effect of the material to be welded degraded; thereby, F_z force became higher. For the 2198 Al–Li alloy, select welding parameters generate more frictional heat to reduce adverse effects on the robot.

3.2. Mechanical Property of 2198 Al–Li Alloy Made with Robotic FSW

The strain–stress curves of 2198 weldments made with robotic FSW are shown in Figure 4. It shows that the elastic deformation phases of all welds were similar, while the plastic deformation phases differed from each other. With welding speed increasing, the tensile strength first increased and then decreased. The highest tensile strength of 384 MPa, which is 88% of base metal, was obtained at the welding speed of 100 mm/min.

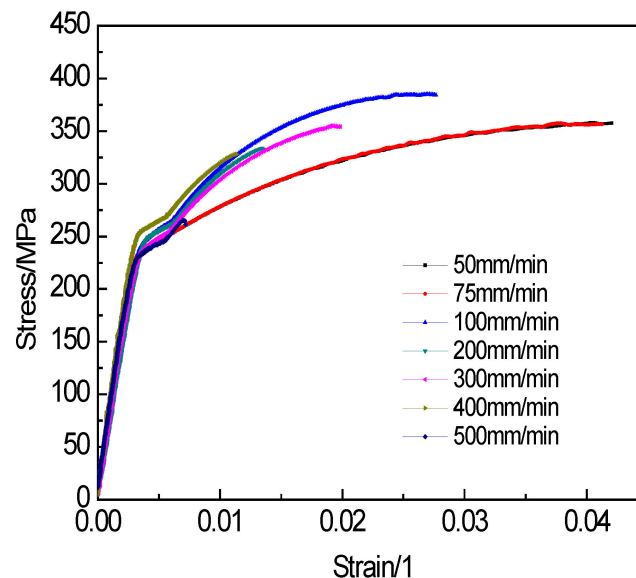


Figure 4. Strain–stress curves of robotic FSW 2198 Al–Li alloys joints.

As welding speed grew faster, the heat input per time increased, and maximum temperature during welding heightened. When the welding temperature was relatively lower, the plasticized materials flowed badly and probably did not refill the cavity behind the tools, resulting in a weak connection. On the other hand, if the heat input was too high, the plasticized materials stirred excessively and probably flowed outwards of the weldment, resulting in joint degradation [24].

The relationship between welding speed and ultimate strain is shown in Figure 5, which shows that the engineering strain approximately decreased as the welding speed increased.

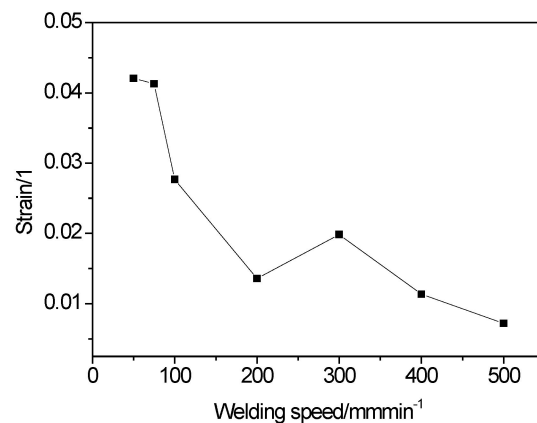


Figure 5. Overall engineering strain of robotic FSW 2198 Al–Li alloys.

The micro-hardness variations along the centerline on crossing sections of robotic FSW 2198 welds at different welding speeds are demonstrated in Figure 6. It can be seen that the micro-hardness curves of all welds are almost symmetric along the weld centerline and presented a W-shape, and the micro-hardness of the advancing side is relatively higher than that of the retreating side. The micro-hardness of the base metal is higher than the weldment, with the maximum value of approximately 159 HV. However, the micro-hardness within the weldment decreased significantly, and the minimum value stands at 70 HV.

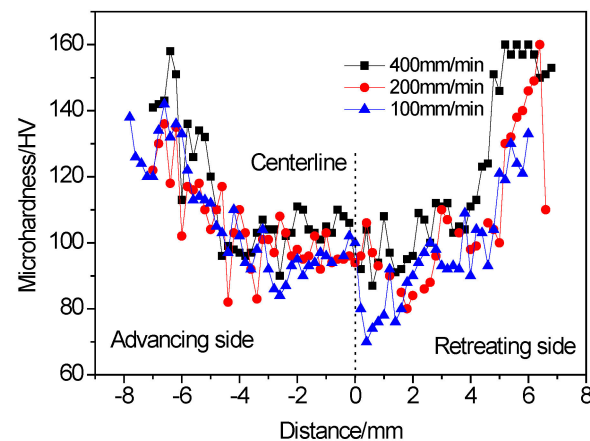


Figure 6. Micro-hardness distribution on crossing section of welds at various welding speeds.

In addition, by comparing the curves of different welding speeds, it can be seen that as the welding speed decreases, the microhardness decreases. The micro-hardness of weld at a welding speed of 400 mm/min is about 15 HV higher than that of the weld with a welding speed of 100 mm/min, as shown in Figure 5. Of all micro-hardness curves, the micro-hardness in the nugget zone increased to some extent, and the lowest value was located at the thermo-affected zone. Schneider J. has studied the hardness distribution of FSW 2198-T8 alloy and found a similar trend. The precipitation behavior of different zones contributed to the trend [25].

3.3. Cross-Section Microstructure of Al–Li Alloy Made with Robotic FSW

The 3D microstructure of base metal showed that anisotropy was affected by rolling processing, as demonstrated in Figure 7a. The EBSD test of the crossing section of base metal is given in Figure 7b: elongation grains with a size of 200–300 μm in length and 60–120 μm in width can be seen.

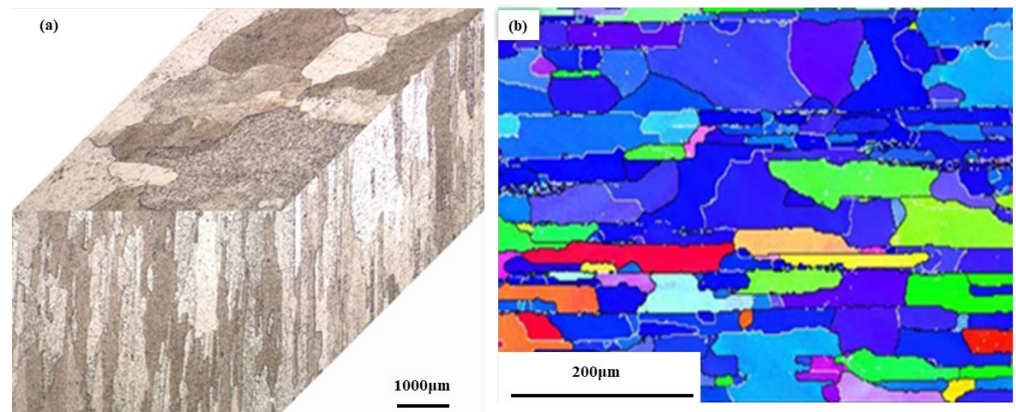


Figure 7. Microstructure of base metal in 3D and EBSD map of crossing section (a) A 3D demonstration of base metal; (b) EBSD investigation of crossing section microstructure of base metal.

The cross-microstructure of robotic FSW 2198 at 100 mm/min is given in Figure 8. There are three areas in weld joints, including the nugget zone, thermo-mechanically affected zone, and heat-affected zone, as shown in Figure 8a. The nugget zone consisted of refined equiaxed grains, as shown in Figure 8c. The EBSD test demonstrated that the average grain size in the nugget zone is 10 µm, much smaller than that of the base metal. The refined grains were related to the recrystallization caused by severe deformation and high temperature during the FSW process [26–28].

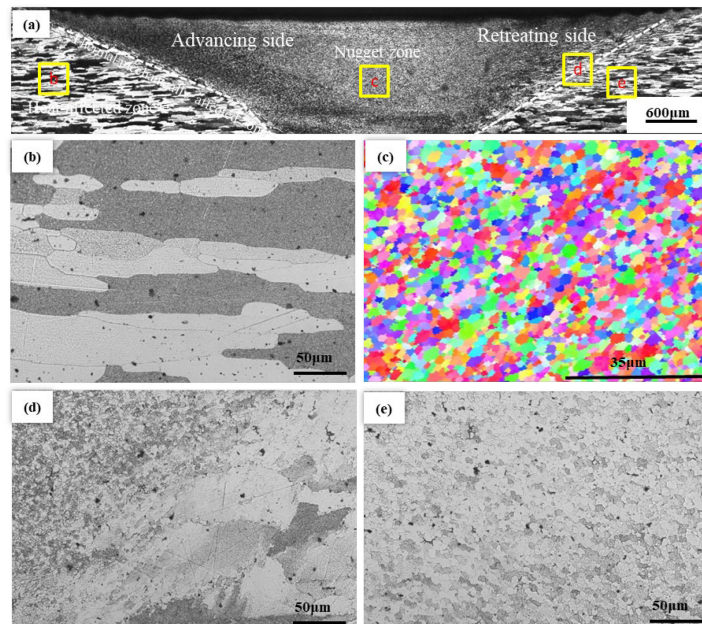


Figure 8. Microstructure of robotic FSW 2 mm 2198 Al-Li alloys: (a) overall microstructure; (b) base metal; (c) nugget zone; (d) thermo-mechanically affected zone; (e) heat affected zone.

The grain size in the nugget zone depended on strain rate and deformation temperature. These two variables can be expressed by the Zener–Hollomon parameter (Z) as [25]:

$$Z = \dot{\epsilon} \exp \left[\frac{Q}{RT} \right] \quad (3)$$

where $\dot{\epsilon}$ is the strain rate; Q is the activation energy of the process; R is the universal gas constant and T is the deformation temperature [29,30].

$$\dot{\epsilon} = \frac{\epsilon}{t}$$

where ϵ is strain, and t is deformation time. The total strain during processing can be described as

$$\epsilon = \ln\left(\frac{l}{APR}\right) + \left| \ln\left(\frac{APR}{l}\right) \right|$$

where APR is the tool advance per revolution (mm/min), and l might be expressed as

$$l = 2r \cos^{-1}\left[\frac{r-a}{r}\right]$$

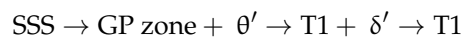
$$d_{DRZ} = CZ^\delta$$

where, C and δ are material constants. Theoretical calculation showed that the grain size of the nugget zone was 18.4 μm , which was close to the practical measurement value of 10 μm .

Grains in the thermo-mechanically affected zone are elongated and bend along the rotating direction, as shown in Figure 8d. Grains in the heat-affected zone only experienced friction heat effect without deformation, so they grew a little compared to the base metal, as demonstrated in Figure 8b.

3.4. TEM Observation of Robotic FSW 2198 Al–Li Alloys

The TEM observation of the base metal, nugget zone, and heat-affected zone is demonstrated in Figure 9. In the third generation Al–Li alloys, with addition of Cu, which was less than 5%, the main precipitation sequence is as follows:



The main precipitate was the GP zone, T1 and δ' . It can be seen that in the base metal, there is a large number of acicular T1 precipitates in Figure 9a.

After FSW, the grains in the nugget zone experienced severe deformation and high friction temperature, which lead to recrystallization into refined grains, as shown in Figure 9b. The T1 precipitation disappeared, and a certain amount of δ' and dislocation could be found within grains, as illustrated by arrows.

Precipitation in the heat-affected zone showed that there is T1 precipitation in this area, as shown in Figure 9d. The grains in these zones only underwent friction heat, so the T1 precipitation also can be seen in this area as a relatively small amount, and θ' precipitation disappeared; δ' precipitation remained.

T1 is the predominant strengthening phase in the alloy. It presents as plates on $\langle 111 \rangle$ planes in the matrix and can be identified easily from the reflections in the SADP [31]. The four symmetrical spots at $1/3 \langle 220 \rangle$ in the [100] SADP, as shown in Figure 9e, and the reflections in the [211] SADP, as shown in Figure 9f, can prove the existence of T1.

In 2198 Al–Li alloys, the high strength comes from grain boundary strengthening σ_{gb} , precipitation strengthening σ_{ppt} , and solid solution strengthening σ_{SSS} . After FSW, the nugget zone consists of fine recrystallization grains with an average size of 10 μm , which was much smaller than that of the base metal. According to the Hall-Petch equation:

$$\sigma_{gb} = K/\sqrt{d}$$

where d is the average grain size of the matrix, and k is a constant for Al–Li alloys.

The hardness and tensile strength would be much higher than that of the base metal; however, the hardness showed that the hardness value of the nugget zone was lower than

the base metal. This was mainly due to the disappearance of precipitation in the nugget zone, as shown in Figure 9b. The increase in hardness value could not offset the decrease caused by T1, and δ' precipitation disappeared. Therefore, the hardness value of the nugget zone is lower than that of the base metal.

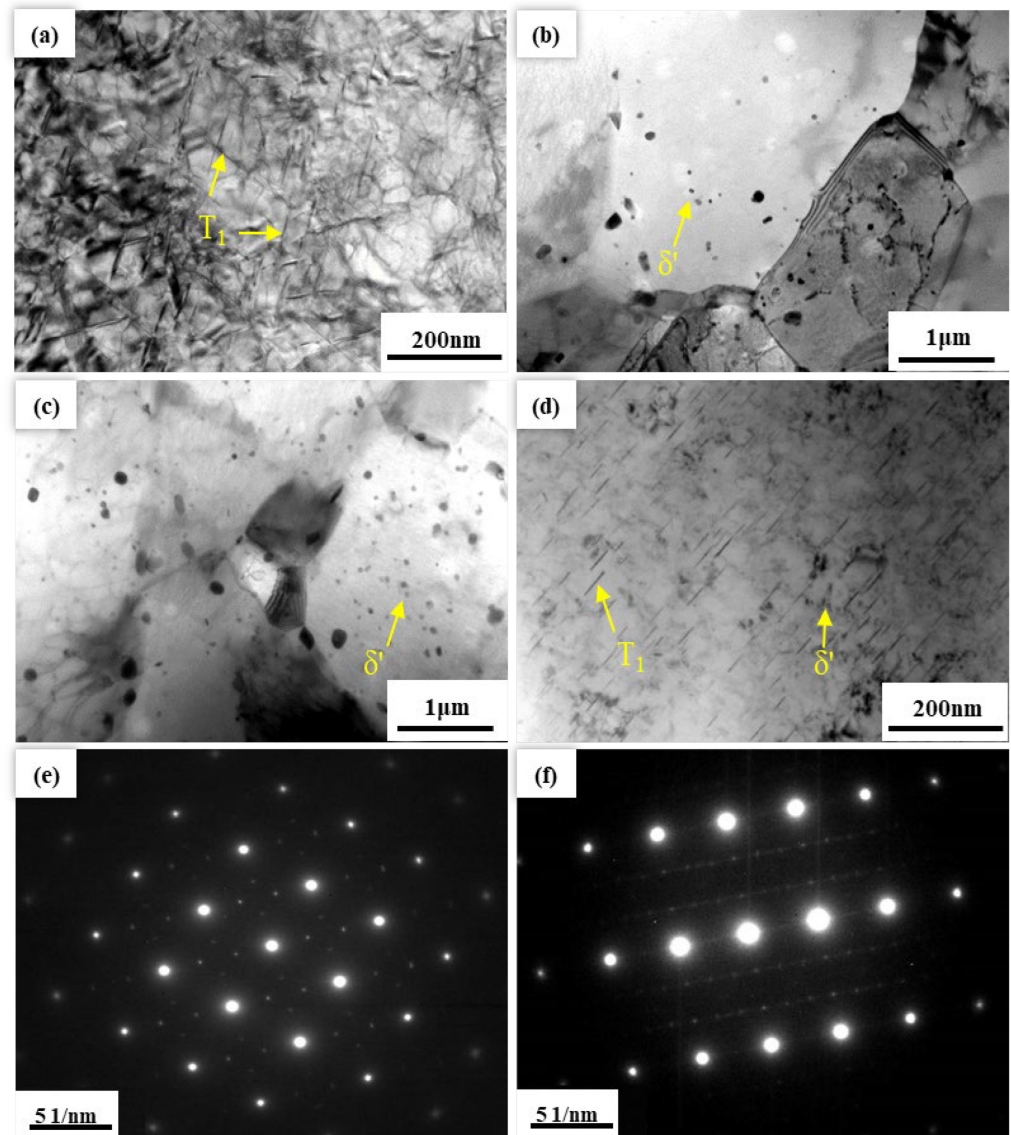


Figure 9. TEM observation of microstructure of (a) base metal; (b,c) nugget zone; (d) heat-affected zone. (e) SADPS for nugget zone [100]; (f) SADPS for nugget zone [211].

3.5. Fracture Observation of Robotic FSW 2198Al–Li Alloys

The morphology of tensile test samples at welding speeds of 50 mm/min, 200 mm/min and 500 mm/min is given in Figure 10. An ultimate strain of 0.042 was obtained at a welding speed of 50 mm/min. The flat fracture surface and local river-like patterns can be seen. The fracture surface also shows many petal-like rip edges and cleavage planes. It can be concluded that the fracture is a quasi-cleavage fracture.

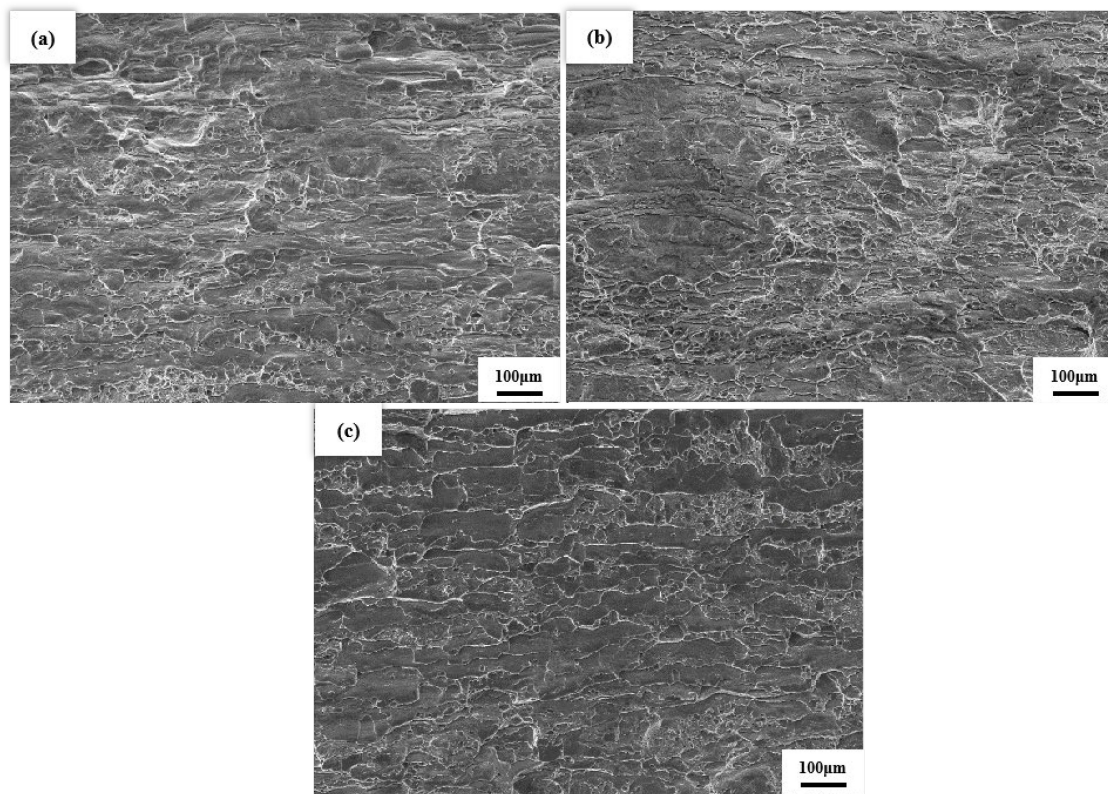


Figure 10. Fracture surface of robotic FSW of 2198 Al–Li alloys: (a) welding speed of 50 mm/min; (b) welding speed of 200 mm/min; (c) welding speed of 500 mm/min.

For the sample welding at 200 mm/min, the morphology of fracture showed a river-like pattern on the fracture surfaces. The quasi-cleavage facets on the fracture surface can be seen from its microscopic fracture picture. These quasi-cleavage facets are connected with rip edges. It can be concluded that fracture of this specimen is a quasi-cleavage fracture.

For the sample welding at 500 mm/min, the ultimate strain is about 0.01, and the sample macroscopically exhibits brittle fracture.

4. Conclusions

A 2 mm 2198 Al–Li plate was successfully friction stir-welded using an industrial robot at different welding speeds.

- (1) As welding speeds increased from 50 mm/min to 500 mm/min, F_z increased significantly from about 3.8 KN to 8.4 KN in the stable welding stage;
- (2) The tensile strength first increased and then decreased as welding speed increased, and maximum tensile strength was 384 MPa when the welding speed was 100 mm/min, the overall ultimate strain decreased along with welding speed increasing.
- (3) The grains in the nugget zone turned from elongated rolling grains to refined recrystallization grains, and its grains size depends on strain rate and deformation temperature.
- (4) A W-shape asymmetric hardness curve was obtained in the weld joints. The micro-hardness decreased compared with the base metal. The lowest hardness values were obtained in the thermo-mechanically affected zone due to the coarsening of precipitates.
- (5) In the base metal, T1 and δ' precipitations were located evenly, while in the nugget zone of weldment, only a few δ' remained, as most of the T1 and δ' dissolved into the matrix.

Author Contributions: Conceptualization, H.J.; methodology, Y.W. and Q.M.; validation, X.W.; formal analysis, Y.W. and X.W.; investigation, Y.W.; resources, Q.M.; data curation, Y.W. and X.W.; writing—original draft preparation, Y.W.; writing—review and editing, H.J. and X.W.; visualization, Q.M.; supervision, H.J.; project administration, H.J. and Q.M.; funding acquisition, H.J. All authors have read and agreed to the published version of the manuscript.

Funding: This research received no external funding.

Conflicts of Interest: The authors declare no conflict of interest.

References

- De Backer, J.; Christiansson, A.K.; Oqueka, J.; Bolmsjö, G. Investigation of path compensation methods for robotic friction stir welding. *Ind. Robot. Int. J.* **2012**, *39*, 601. [[CrossRef](#)]
- Lukin, V.I.; Erasov, V.S.; Panteleev, M.D.; Avtaev, V.V.; Samorukov, M.L.; Kulik, V.I. Friction stir welding of aircraft wings. *Weld. Int.* **2018**, *32*, 690–694. [[CrossRef](#)]
- Shi, L.; Dai, X.; Tian, C.; Wu, C. Effect of splat cooling on microstructures and mechanical properties of friction stir welded 2195 Al–Li alloy. *Mater. Sci. Eng. A* **2022**, *858*, 144169. [[CrossRef](#)]
- Giummarra, C.; Rioja, R.J.; Bray, G.H.; Magnusen, P.E.; Moran, J.P. Al–Li alloys: Development of corrosion resistant, high toughness aluminium–lithium aerospace alloys. In Proceedings of the ICAA11 Conference, Aachen, Germany, 22 September 2008–26 September 2008; Volume 1, pp. 176–188.
- Heinz, A.; Haszler, A.; Keidel, C.; Moldenhauer, S.; Benedictus, R.; Miller, W.S. Recent development in aluminium alloys for aerospace applications. *Mater. Sci. Eng. A* **2000**, *280*, 102–107. [[CrossRef](#)]
- Knuwer, M.; Schumacher, J.; Ribes, H.; Eberl, F.; Bes, B. 2198–Advanced Aluminium–Lithium alloy for A350 skin sheet application. In Proceedings of 17th AeroMat Conference & Exposition, Seattle, WA, USA, 15–18 May 2006.
- Chen, Y.C.; Liu, H.J.; Feng, J.C. Effect of post-weld heat treatment on the mechanical properties of 2219–O friction stir welded joints. *J. Mater. Sci.* **2006**, *41*, 297–299. [[CrossRef](#)]
- Smith, C.B.; Hinrichs, J.F.; Crusan, W.A. Robotic friction stir welding: The state of the art. In Proceedings of the 4th International Symposium of Friction Stir Welding, Park City, UT, USA, 14–16 May 2003.
- Bres, A.; Monsarrat, B.; Dubourg, L.; Birglen, L.; Perron, C.; Jahazi, M.; Baron, L. Simulation of friction stir welding using industrial robots. *Ind. Robot. Int. J.* **2010**, *37*, 36. [[CrossRef](#)]
- Huang, Y.X.; Wan, L.; Lv, S.X.; Zhang, J.; Fu, G.S. In situ rolling friction stir welding for joining AA2219. *Mater. Des.* **2013**, *50*, 810–816. [[CrossRef](#)]
- Ji, S.D.; Xiang, J.W.; Yue, Y.M.; Ma, Y.N.; Zhang, L.G.; Gao, S. Design of friction stir welding tool for avoiding root flaws. *Materials* **2013**, *6*, 5870–5877. [[CrossRef](#)]
- Aziz, S.B.; Dewan, M.W.; Huggett, D.J.; Wahab, M.A.; Okeil, A.M.; Liao, T.W. A fully coupled thermomechanical model of friction stir welding (FSW) and numerical studies on process parameters of lightweight aluminum alloy joints. *Acta Metall. Sin.* **2018**, *31*, 1–18. [[CrossRef](#)]
- Liu, G.; Ma, L.N.; Ma, Z.D.; Fu, X.S.; Wei, G.B.; Yang, Y.; Xu, T.C.; Xie, W.D.; Peng, X.D. Effects of welding speed and post-weld hot rolling on microstructure and mechanical properties of friction stir-welded AZ31 magnesium alloy. *Acta Metall. Sin.* **2018**, *31*, 853–864. [[CrossRef](#)]
- Bakhtiari Argesi, F.; Shamsipur, A.; Mirsalehi, S.E. Dissimilar joining of pure copper to aluminum alloy via friction stir welding. *Acta Metall. Sin.* **2018**, *31*, 1183–1196. [[CrossRef](#)]
- Wei, S.; Hao, C.; Chen, J. Study of friction stir welding of 01420 aluminum–lithium alloy. *Mater. Sci. Eng. A* **2007**, *452–453*, 170–177. [[CrossRef](#)]
- Cavaliere, P.; Cabibbo, M.; Panella, F.; Squillace, A. 2198 Al–Li plates joined by friction stir welding: Mechanical and microstructural behavior. *Mater. Des.* **2009**, *30*, 3622–3631. [[CrossRef](#)]
- Cavaliere, P.; Santis, A.D.; Panella, F.; Squillace, A. Effect of anisotropy on fatigue properties of 2198 Al–Li plates joined by friction stir welding. *Eng. Fail. Anal.* **2009**, *16*, 1856–1865. [[CrossRef](#)]
- Chen, J.; Madi, Y.; Morgeneyer, T.F.; Besson, J. Plastic flow and ductile rupture of a 2198 Al–Cu–Li aluminum alloy. *Comput. Mater. Sci.* **2011**, *50*, 1365–1371. [[CrossRef](#)]
- Cisko, A.R.; Jordon, J.B.; Amaro, R.L.; Allison, P.G.; Wlodarski, J.S.; McClelland, Z.B.; Garcia, L.; Rushing, T.W. A parametric investigation on friction stir welding of Al–Li 2099. *Mater. Manuf. Process.* **2020**, *35*, 10. [[CrossRef](#)]
- Chen, P.; Chen, J.; Qin, S.; Zou, S.; Song, S.; Jiang, T.; Zhang, Z.; Jia, Z.; Liu, Q. Friction stir welding joints of 2195–T8 Al–Li alloys: Correlation of temperature evolution, microstructure and mechanical properties. *Mater. Sci. Eng. A* **2021**, *823*, 141501.
- Chen, S.-j.; Kong, D.-b.; Dong, J.-t.; Jiang, X.-q.; Yuan, T. Influence of process parameters on axial force and transverse force of robot friction stir welding. *Chin. J. Nonferrous Met.* **2021**, *31*, 956–967.
- Chao, Y.J.; Qi, X.; Tang, W. Heat transfer in friction stir welding—Experimental and numerical studies. *J. Manuf. Sci. Eng.* **2003**, *125*, 138–145. [[CrossRef](#)]
- Arbegast, W.J.; Hartley, P.J. Characteristics of friction stir welded aluminum alloys. In Proceedings of the Fifth International Conference on Trends in Welding Research, Pine Mountain, GA, USA, 1–5 June 1998; p. 541.

24. Ji, S.D.; Meng, X.C.; Huang, Y.Y. Effect of rotational velocity of tool on mechanical properties of stationary shoulder friction stir welding. *Trans. China Weld. Inst.* **2015**, *36*, 51–54.
25. Nandan, R.G.G.R.; Roy, G.G.; Lienert, T.J.; Debroy, T. Three-dimensional heat and material flow during friction stir welding of mild steel. *Acta. Mater.* **2007**, *55*, 883. [[CrossRef](#)]
26. Sato, Y.S.; Kokawa, U.M.H. Parameters controlling microstructure and hardness during friction-stir welding of precipitation-hardenable aluminum alloy. *Metal. Mater. Trans. A* **2002**, *33*, 625–635. [[CrossRef](#)]
27. Kwon, Y.J.; Shigematsu, I.; Saito, N. Mechanical properties of fine-grained aluminum alloy produced by friction stir process. *Scr. Mater.* **2003**, *49*, 785–789.
28. Liang, X.P.; Li, H.Z.; Li, Z.; Hong, T.; Ma, B.; Liu, S.D.; Liu, Y. Study on the microstructure in a friction stir welded 2519-T87 Al alloy. *Mater. Des.* **2012**, *35*, 603–608. [[CrossRef](#)]
29. Reynolds, A.P. Flow visualization and simulation in FSW. *Scr. Mater.* **2008**, *58*, 338. [[CrossRef](#)]
30. Liu, X.Q.; Liu, H.J.; Wang, T.H.; Wang, H.G.; Yang, S. Correlation between microstructures and mechanical properties of high-speed friction stir welded aluminum hollow extrusions subjected to axial forces. *J. Mater. Sci. Technol.* **2018**, *34*, 102–111. [[CrossRef](#)]
31. Zhang, J.; Feng, X.S.; Gao, J.S.; Huang, H.; Ma, Z.Q.; Guo, L.J. Effects of welding parameters and post-heat treatment on mechanical properties of friction stir welded AA2195-T8 Al-Li alloy. *J. Mater. Sci. Technol.* **2018**, *34*, 219–227. [[CrossRef](#)]

Disclaimer/Publisher’s Note: The statements, opinions and data contained in all publications are solely those of the individual author(s) and contributor(s) and not of MDPI and/or the editor(s). MDPI and/or the editor(s) disclaim responsibility for any injury to people or property resulting from any ideas, methods, instructions or products referred to in the content.